Ocean dynamics of outer solar system satellites

K. M. Soderlund[1]

[1]Institute for Geophysics, Jackson School of Geosciences, The University of Texas at Austin, Austin, Texas, USA

Key Points:

- Ocean dynamics are important for the habitability of icy ocean worlds.
- Strong ocean currents likely exist in Enceladus, Titan, Europa, and Ganymede.
- Convective heat transfer in the ocean is predicted to vary with latitude, which would modify the thermophysical structure of the ice shell.

Corresponding author: Krista Soderlund, krista@ig.utexas.edu

Abstract
Ocean worlds are prevalent in the solar system. Focusing on Enceladus, Titan, Europa, and Ganymede, I use rotating convection theory and numerical simulations to predict ocean currents and the potential for ice-ocean coupling. When the influence of rotation is relatively strong, the oceans have multiple zonal jets, axial convective motions, and most efficient heat transfer at high latitudes. This regime is most relevant to Enceladus and possibly to Titan, and may help explain their long-wavelength topography. For a more moderate rotational influence, fewer zonal jets form, Hadley-like circulation cells develop, and heat flux peaks near the equator. This regime is predicted for Europa, where it may help drive geologic activity via thermocompositional diapirism in the ice shell, and is possible for Titan. Weak rotational influence allows concentric zonal flows and overturning cells with no preferred orientation. Predictions for Ganymede's ocean span multiple regimes.

Plain Language Summary: The outer solar system is host to a large number of diverse satellites, many of which likely have global oceans beneath their outer icy shells. I use theoretical arguments and numerical models to make predictions about ocean currents and heat transfer across such oceans. Our results suggest that strong ocean currents exist in Enceladus, Titan, Europa, and Ganymede, and cause the transfer of heat to vary with latitude that may modify the overlying ice shell.

1 Introduction

Exploration of the outer solar system has shown that subsurface oceans may be relatively common in the interiors of icy satellites and dwarf planets (Nimmo & Pappalardo, 2016; Lunine, 2017). Strong evidence exists for oceans in the Saturnian satellites Enceladus and Titan, with oceans also potentially present in Mimas and Dione. In the Jovian system, there is compelling evidence for a Europan ocean and oceans are predicted within Ganymede and potentially Callisto as well (c.f. Hartkorn & Saur, 2017). Kuiper belt objects, such as Pluto, Charon, and the Neptunian satellite Triton, may also have subsurface oceans.

The presence of liquid water makes these ocean worlds compelling astrobiological targets. However, the dynamics of these oceans also play a role in promoting habitable environments. For example, heat and material exchange between the seafloor and ice shell will be enhanced if the ocean is unstable to convection (e.g., Vance & Goodman, 2009; Soderlund et al., 2014), has mechanically driven flows (e.g., Tyler, 2008; Lemasquerier et al., 2017; Wilson & Kerswell, 2018; Rovira-Navarro et al., 2019), or has fluid motions driven by magnetic pumping (Gissinger & Petitdemange, 2019). Currents and turbulence tend to mix the ocean waters, which implies the presence of strong thermal and compositional gradients near the top and bottom of the ocean that life may take advantage of. Mixing efficiency may vary spatially, so these motions are also important for the distribution of potential bionutrients. In addition, heat transfer from the ocean will influence where the ice shell melts and freezes. Melting of the ice shell and freezing of the ocean will impact the salt budget, especially near the ice-ocean interface, a habitable environment in analogous terrestrial ice shelves (e.g., Daly et al., 2013). Moreover, accreted ice depleted in salts may have positive buoyancy and lead to upwelling thermocompositional diapirs in the ice shell that would link the surface and subsurface (e.g., Pappalardo & Barr, 2004; Soderlund et al., 2014).

Here, I focus on the ocean dynamics of Enceladus and Titan given the abundance of data from the *Cassini* mission and of Europa and Ganymede in preparation for the upcoming *Europa Clipper* (Phillips & Pappalardo, 2014) and *JUICE* (Grasset et al., 2013) missions. Scaling laws for rotating convection systems are used to make predictions about their convective behaviors in Section 2, and numerical models of global ocean convection characterizing the predicted regimes are presented in Section 3. Implications for icy

satellites are explored in Section 4, and the challenges of extrapolating to realistic ocean conditions are discussed in Section 5.

2 Rotating Convection Scaling Laws

Convection characteristics depend critically on the relative importance of rotation, which tends to organize the fluid into columns aligned with the rotation axis, increase the critical Rayleigh number, constrain heat transfer efficiency, and drive zonal flows (e.g., Aurnou et al., 2015). Cheng et al. (2018) combines asymptotic predictions, laboratory experiments, and numerical simulations to review the behavior of rotating thermal convection as a function of the dimensionless Ekman, Rayleigh, and Prandtl numbers. The Ekman number, $E = \nu/2\Omega D^2$, represents the ratio of rotational to viscous timescales; thus, low E signifies rapid rotation rates in planetary interiors. The Rayleigh number, $Ra = \alpha g \Delta T D^3/\nu\kappa$, is the ratio of the thermal diffusion time to the viscous buoyant rise time; large Ra denotes strong buoyancy forcing. The Prandtl number, $Pr = \nu/\kappa$, defines the ratio of thermal to viscous diffusion timescales. Here, ν is kinematic viscosity, Ω is rotation rate, D is ocean thickness, α is thermal expansivity, g is gravitational acceleration, ΔT is superadiabatic temperature contrast, and κ is thermal diffusivity.

Cheng et al. (2018) identify five rotating convection regimes: columnar, plumes, geostrophic turbulence (GT), unbalanced boundary layer (UBL), and nonrotating heat transfer (NR) (see Fig. 1). Near onset, convection in the bulk fluid manifests as Taylor columns aligned with the rotation axis ("columnar" regime). With increased buoyancy forcing, the columns begin to deteriorate such that they no longer extend fully across the fluid layer ("plumes" regime). Convection eventually becomes vigorous enough for strong mixing in the bulk fluid ("geostrophic turbulence" regime). Despite the disappearance of coherent vertical structures, the Coriolis force still imposes a vertical stiffness on the flow field. These regimes are shown collectively on Figure 1. The influence of rotation is lost locally at Rayleigh numbers exceeding Ra_{GTU}, which corresponds to the breakdown of geostrophy (balance between Coriolis and pressure gradient forces) in the thermal boundary layers ("unbalanced boundary layers" regime). For Rayleigh numbers greater than Ra_{UNR}, the influence of rotation is lost globally ("nonrotating heat transfer" regime). As reviewed by Cheng et al. (2018), significant debate exists in the community on the scaling laws for Ra_{GTU} and Ra_{UNR}. Rather than assume a single scaling law for each transition, I consider upper and lower bound scaling laws for each regime and highlight the resulting range of parameter space for each regime transition in Figure 1.

Using this regime diagram, one can predict the convective regime of a system if the Ekman, Rayleigh, and Prandtl numbers can be estimated (see Table 1). The Prandtl number depends only on fluid properties and is estimated to be $Pr \sim 10$ for the satellite oceans (Abramson et al., 2001; Nayar et al., 2016). The Ekman number is also relatively easy to calculate since it only requires assumptions about the fluid viscosity, rotation rate, and ocean thickness. I use the internal structure models of Vance et al. (2018) (see their Tables 5-8) to obtain ocean thicknesses D_{ocean} for six combinations of possible outer ice shell thicknesses and ocean compositions for each satellite. Enceladus' ocean has the largest Ekman number of $E \sim \mathcal{O}(10^{-10})$, while the ocean of Ganymede has the lowest at $E \sim \mathcal{O}(10^{-13})$.

The Rayleigh number is more difficult to estimate because it requires knowledge of the superadiabatic temperature contrast ΔT. One can derive an estimate, however, using the relationship between the Rayleigh number and the convective heat transfer efficiency as measured by the Nusselt number, $Nu = qD/\rho C_p \kappa \Delta T$. Following Soderlund et al. (2014), I leverage $Nu{-}Ra$ scalings to solve for ΔT algebraically and consider both non-rotating and rapidly rotating scaling laws to give end-member estimates. More recent scaling laws for rotating spherical shells are used here, however. In the non-rotating

regime, heat transfer is expected to be independent of the Ekman number and follow the theoretical limit of $Nu = 0.07Ra^{1/3}$ (e.g., Gastine et al., 2015). Conversely, in the rapidly rotating limit, heat transfer is predicted to follow $Nu = 0.15Ra^{3/2}(2E)^2$ (Gastine et al., 2016). As a result, the temperature contrast is given by

$$\Delta T = 7.3 \left(\frac{\nu}{\alpha g \rho C_p} \right)^{1/4} q^{3/4} \tag{1}$$

in the non-rotating regime and by

$$\Delta T = 2.1 \left(\frac{\Omega^4 \kappa}{\rho^2 C_p^2 \nu \alpha^3 g^3} \right)^{1/5} (q^2 D)^{1/5} \tag{2}$$

in the rapidly-rotating regime.

Here, I assume the heat flux q from each of the six interior models per satellite, noting that the lower q estimates are associated with thicker ice Ih shells (Vance et al., 2018). Although these values are generally consistent with the literature, the minimum heat fluxes tend to exceed those predicted for radiogenic heating in the mantle at present day (e.g., Bland et al., 2009) and the upper bound for Ganymede is appropriate for a past active period (e.g., Dombard & McKinnon, 2001). If q is decreased by an order of magnitude, the lower bounds for ΔT, and therefore Ra, only decrease by a factor of 2.5 per eqn. (2). Our global estimates also neglect spatial variations in heat flow that may be locally strong at Enceladus (Choblet et al., 2017), for example, where narrow mantle upwellings can reach $1-5$ W/m^2 (the global average, however, is in line with Vance et al. (2018)). If q is increased by an order of magnitude, the Ra upper bounds increase by a factor 5.6 per eqn. (3). As shown in Table 1, Rayleigh numbers span from $Ra \sim \mathcal{O}(10^{16})$ for the lower Enceladus limit to $Ra \sim \mathcal{O}(10^{24})$ for the upper Ganymede limit. An important caveat to note here, however, is that these estimates do not include compositional contributions due to salinity gradients. This simplification may be especially significant for Titan since the ocean is hypothesized to have a high concentration of dissolved salts (Baland et al., 2014; Mitri et al., 2014).

Figures 1 and S1 plot the resulting estimates of the Ekman and Rayleigh numbers on the convective regime diagram. The oceans of Titan, Europa, and Ganymede are predicted to behave similarly since their estimated parameter spaces have considerable overlap. Since these estimates fall near the lower boundary between the UBL and NR regimes, I hypothesize that rotational effects do not dominate the turbulent local-scale convective flows. Conversely, rotation likely has a stronger influence on the ocean of Enceladus, which is also predicted to be primarily in the UBL regime, although extending into the GT transition.

3 Numerical Convection Models

Numerical models of global ocean convection are next used to characterize the currents and heat flow patterns. I utilized the pseudospectral code MagIC, version 5.6 (e.g., Wicht, 2002; Gastine & Wicht, 2012) to simulate 3D, time-dependent, thermal convection of a Boussinesq fluid in a rotating spherical shell with geometry characterized by the ratio of inner to outer shell radii, $\chi = r_i/r_o = 0.9$. The system is further defined by the Ekman, Rayleigh, and Prandtl numbers. Following Soderlund et al. (2014), the boundaries are impenetrable, stress-free, and isothermal. Compositional buoyancy, spatial variations in mantle heat flow, and mechanically driven flows are neglected for simplicity.

Seven models that span a convective regime space consistent with the icy satellite ocean predictions are considered (Fig. 1). In the first series, the Rayleigh and Prandtl numbers are fixed to $Ra = 3.4 \times 10^7$ and $Pr = 1$, and the Ekman number is increased

from $E = 3.0 \times 10^{-5}$ to $E = 7.5 \times 10^{-4}$. The second series of models increase the Rayleigh number from $Ra = 2.4 \times 10^6$ to $Ra = 3.4 \times 10^7$ for fixed $E = 1.5 \times 10^{-4}$ and $Pr = 1$; higher Ra values were not pursued to due computational limitations. Hyperdiffusivities are not employed (c.f. Zhang & Schubert, 2000). The numerical grids have 73 radial points, 320 latitudinal points, and 640 longitudinal points for cases with $E \geq 7.5 \times 10^{-5}$ and 65 radial points, 640 latitudinal points, and 1280 longitudinal points for the $E = 3.0 \times 10^{-5}$ case. Each model was initiated with a random temperature perturbation or restarted from a lower E or Ra case.

Figure 2 shows the mean velocity and temperature fields of each model across the E parameter sweep, while Figure 3 shows the normalized heat flux along the outer boundary. In the highest Ekman number case (Fig. 2a), the zonal and radial flows have comparable magnitudes reminiscent of non-rotating convection. The radial flows have no preferred spatial orientation, while the zonal flows are concentric due to viscous transport of angular momentum (Brun & Palacios, 2009). Ocean temperatures are nearly isothermal away from the boundaries, leading to localized heat flux perturbations along the ice-ocean interface (Fig. 3a).

When the Ekman number is decreased (Fig. 2b-c), homogenization of absolute angular momentum leads to zonal flows that are retrograde (westward) at large cylindrical radii and prograde (eastward) closer to the rotation axis (e.g., Gilman, 1978; Aurnou et al., 2007; Gastine et al., 2013). The mean radial flows become more organized with a pronounced upwelling near the equator and downwellings at mid-latitudes, essentially forming Hadley-like meridional circulation cells in each hemisphere. Upon further decreasing of the Ekman number (Fig. 2d), multiple zonal jets that alternate in direction develop, and the mean radial flows retain an equatorial upwelling that becomes more aligned with the rotation axis. Both mean zonal and radial flow speeds decrease by a factor of five compared to the $E = [3.0, 1.5] \times 10^{-4}$ cases. In all three of these models (Fig. 2b-d), ocean temperatures are characterized by thin thermal boundary layers and warmer equatorial waters. Heat flux peaks at low latitudes (with minima at mid-latitudes) due to the mean overturning circulations with secondary peaks forming at high latitudes due to turbulent heat transfer associated with vertically ascending plumes (Fig. 3b-d).

In the lowest Ekman number case (Fig. 2e), Coriolis forces organize the flow into narrow structures that are aligned with the rotation axis. Reynolds stresses associated with these columns drive prograde equatorial flow with jets that alternate in direction at higher latitudes due to correlation locally between the azimuthal and cylindrically radial flow components (e.g., Aurnou & Olson, 2001; Christensen, 2001; Heimpel et al., 2005; Gastine et al., 2014). Ocean temperatures are not well-mixed, especially at low latitudes, due to the axialized convective flows and strong equatorial jet (e.g., Aurnou et al., 2008). Consequently, heat flow along the ice-ocean interface peaks at high latitudes with minima near the equator (Fig. 3e).

A similar trend from three-jet zonal flows, equatorial upwelling, and peak low latitude heat flux to multiple zonal jets, axialized convective flows, and peak high latitude heat flux is found as Ra is decreased (Figs. S2 and S3).

4 Implications for Icy Satellites

In order to apply these models to icy satellite oceans, I assume that the velocity and temperature patterns extrapolate to more extreme parameters following the relative distance between regime boundaries (Fig. S1). Enceladus' ocean may then be represented by the $E = [3.0 \times 10^{-5}, 7.5 \times 10^{-5}]$ models since both fall approximately between the GT-UBL regime transition and the lower bound of the UBL-NR transition. In contrast, the oceans of Europa, Ganymede, and Titan depend on the UBL-NR transition scaling used. If $Ra_{UNR}^{RoC=1} = E^{-2}Pr$ (e.g., Gilman, 1977) is assumed, then all of

these oceans are near the center of UBL regime such that the $E = [7.5 \times 10^{-5}, 1.5 \times 10^{-4}]$ models would be most appropriate for these satellites. If the transition instead follows $Ra_{UNR}^{Ga16} = 100(2E)^{-12/7}$ (Gastine et al., 2016), then the $E = 3.0 \times 10^{-4}$ model would best characterize Europa and the $E = [3.0 \times 10^{-4}, 7.5 \times 10^{-4}]$ models would be most pertinent to Titan and Ganymede.

Below, I discuss the implications for each satellite. Regions with high heat flow are presumed to undergo enhanced melting, leading to ice shell thickness variations. However, large thickness disparities can set up a phenomena known as an ice pump (e.g., Lewis & Perkin, 1986) where pressure-induced melting occurs where the ice shell is thick and re-accretes where the ice shell is thin, effectively reducing topography along the base of the ice shell. Since the accretion process is very efficient at excluding impurities in low temperature environments (e.g., Moore et al., 1994; Eicken et al., 1984), this marine ice may be salt-depleted compared to the overlying ice. The ice may, therefore, have positive buoyancy due to the associated thermal and compositional density anomalies and rise toward the surface in the form of convective diapirs (e.g., Pappalardo & Barr, 2004; Soderlund et al., 2014). Alternatively, if the ice pump mechanism is not efficient, the ice shell may be more unstable to convection where it is relatively thick (Travis et al., 2012; Goodman, 2014).

For Enceladus, I predict the zonal flows to be characterized by multiple jets that alternate in direction (Fig. 2A d-e). Converting model velocities to dimensional units $U = \Omega D Ro$, I expect peak zonal speeds of nearly a m/s depending on the ocean thickness assumed. Meridional circulations are predicted to either be strongly aligned with the rotation axis with speeds up to a few mm/s (Fig. 2B e) or be concentrated in a low latitude upwelling with speeds up to a few cm/s (Fig. 2B d). As a result, heat flow along the ice-ocean interface has distinct peaks at either the poles (Figs. 2C e, 3e) or at the equator and the poles secondarily (Figs. 2C d, 3d).

Measurements of Enceladus' shape, gravitational field, and librational motions show that the ice shell is thin below the south pole and thick at the equator, with an intermediate thickness at the north pole (e.g., Čadek et al., 2016; Beuthe et al., 2016). Inverting these measurements to infer the oceanic heat flux along the ice-ocean interface, Čadek et al. (2019) find peak flux near the poles with a minima at the equator. This pattern implies upwelling of warm water at the poles and downwelling of cool water at low latitudes, which may be caused by ocean convection (Fig. 2e) and/or be a consequence of the pattern of tidal heating in the mantle (Choblet et al., 2017). Considering the former, the $E = 3.0 \times 10^{-5}$ model is appropriate if a low internal heat flux is assumed (in contrast to Choblet et al., 2017) or if the thermal expansion coefficient in our calculations is overestimated since α trends towards zero with decreasing salinity and becomes negative for freshwater (e.g., Nayar et al., 2016; Feistel, 2010, see also Table 1), which both effectively reduce the Rayleigh number and make rotational effects more important.

Europa's ocean is predicted to have three zonal jets with retrograde equatorial flow that can reach m/s speeds (Fig. 2A b-c) or multiple zonal jets with retrograde equatorial flow and reduced speeds (Fig. 2A d) depending on the scaling law assumed. All Europa-relevant models, however, have an equatorial upwelling of warm water with peak speeds of roughly a few cm/s and enhanced heat transfer at low latitudes (Figs. 2B-C b-d, 3b-d).

The surface of Europa is riddled with geologic features indicating recent activity and the potential for ocean-derived materials (e.g., Figueredo & Greeley, 2003; Fischer et al., 2015). Chaos terrains, for example, appear to be located preferentially at low latitudes with a secondary prevalence near the poles (Leonard et al., 2018), and formation models suggest that they may be associated with upwelling diapirs (e.g., Sotin et al., 2002; Collins & Nimmo, 2009; Schmidt et al., 2011) and marine ice accretion (Soderlund et

al., 2014). No large gradients in ice shell thickness have been detected (Nimmo et al., 2007), suggesting an efficient ice pump (c.f. Nimmo, 2004). Given our robust model predictions of high oceanic heat flux at low latitudes with relatively low flux at mid-latitudes, our new calculations continue to support the thermocompositional diapirism hypothesis.

Given the similarities in regime predictions for Titan and Ganymede, they are considered together here. Assuming the Ra_{UNR}^{Ga16} scaling and upper Ra estimates, the oceans would behave akin to a non-rotating system with no coherent heat transfer patterns (Figs. 2 C a, 3a). If the lower Ra estimates are instead assumed, these satellites are predicted to have three-jet zonal flows with peak speeds up to a few m/s (depending on ocean thickness), Hadley-like circulation cells with peak speeds up to tens of cm/s (depending on ocean thickness), and maximum heat transfer near the equator (Figs. 2 A-C b, 3b). Alternatively, for the $Ra_{UNR}^{RoC=1}$ scaling, these satellites are predicted to behave similarly to Enceladus and Europa as discussed above (Figs. 2 A-C c-d, 3c-d), except with respect to dimensionalized flow speeds that could be considerably faster due to the larger ocean thicknesses.

Looking to Titan, the satellite's surface topography shows polar depressions compared to relatively elevated low latitudes (e.g., Durante et al., 2019) that are likely explained by ice shell thickness variations (Nimmo & Bills, 2010; Hemingway et al., 2013; Lefevre et al., 2014) or ice shell density variations (Choukroun & Sotin, 2012). As for Enceladus, geophysical measurements by *Cassini* have been used to infer the oceanic heat flux along the ice-ocean interface (Kvorka et al., 2018). The pattern is spatially complex, but simplifies to peaks near the poles when only axisymmetric components are considered. In contrast, the ocean convection models predicted to be relevant for Titan have either no coherent heat flux pattern (Fig. 3a), peak flux and enhanced melting near the equator (Fig. 3b-c), or peak flux near both the equator and the poles (Fig. 3d), none of which are consistent with the observed long-wavelength topography assuming Airy isostasy. If ocean dynamics alone are responsible, this difference implies that either (1) the melted equatorial region in the intermediate scenario was infilled with less dense marine ice to form the equatorial bulge through Pratt isostasy or (2) the ocean has a stably-stratified salinity gradient that reduces the effective buoyancy forcing of the ocean (Ra) such that rotational effects become sufficient to maximize heat flow and melting at the poles (Fig. 3e).

Observational constraints for Ganymede are much more limited. The satellite's ancient grooved terrains indicate a likely period of geologic activity in its early history (Lucchita, 1980) and detection of hydrated salts suggests a subsurface briny layer of fluid (McCord et al., 2001), but no clear patterns are present. Mass anomalies were measured in the northern hemisphere during a single Galileo flyby (Palguta et al., 2006), but the sparsity of data prohibit both characterization on a global scale and unique determination of their depth of origin. Consequently, there is no clear link at present between observations and the underlying ocean dynamics.

5 Discussion

Our results are broadly consistent with the literature. Moreover, by comparing our numerical models against those with different input parameters, we are able to assess their sensitivity to these aspects. For example, the satellite oceans are predicted to have geometries characterized by χ values ranging from 0.74 to 0.99 (Table 1), compared to our models with fixed $\chi = 0.90$. Gastine et al. (2013) found that anelastic columnar convection in thicker spherical shell geometries ($\chi = 0.6$) is also characterized by a prograde equatorial jet with multiple, small-scale meridional circulations aligned with the rotation axis, which transitions to a regime with a retrograde equatorial jet and Hadley cell-like meridional circulations and ultimately a weakening of zonal flow speeds as the influence of rotation is decreased. Similarly, Aurnou et al. (2008) showed that heat trans-

fer is inhibited at low latitudes and generally increases towards the poles for columnar convection in spherical shells with $\chi = [0.85, 0.9]$; this result is different from Miquel et al. (2018), who obtained peak equatorial heat transfer in their asymptotic models of rapidly rotating convection near onset, where the polar regions are subcritical (e.g., Dormy et al., 2004). Conversely, Brun & Palacios (2009) and Soderlund et al. (2013) showed that the equatorial heat transfer enhancement for less vertically stiff convection is robust for thicker shells ($\chi \leq 0.75$) and different thermal boundary conditions. Simulations with thinner spherical shells are computationally demanding and uncommon (c.f. DeRosa et al., 2002). Furthermore, studies with a thin layer of stable stratification below the outer boundary, which may be expected in regions where thermal expansivity is negative (Melosh et al., 2004, see also Table 1), generally show similar trends (e.g., Heimpel et al., 2015). Thus, these studies suggest that our results are not strongly sensitive to variations in ocean thickness or fluid properties with depth. Large spatial variations in ice shell thickness may enhance mechanically driven flows though (e.g., Lemasquerier et al., 2017), which are not considered here.

The effects of different boundary conditions should also be considered. For example, we assumed stress-free mechanical boundaries in order to reduce the effects of viscosity (e.g., artificially large Ekman boundary layers) due to the large E values of our models compared to the satellites (Table 1; Kuang & Bloxham, 1997). In models with no-slip boundary conditions, inertial effects tend to be reduced substantially and strong zonal flows can be inhibited, which can disrupt convection (e.g., Aurnou & Heimpel, 2004; Jones, 2015). For sufficiently driven and rapidly rotating convection, however, no-slip boundaries do not necessarily have this inhibiting effect (Manneville & Olson, 1996; Aubert et al., 2001). Uniform fixed temperature boundary conditions were assumed because they enable a broader comparison with the literature and across the satellites, although fixed heat flux boundary conditions may be more appropriate along the seafloor. At moderate parameters, fixed flux conditions tend to promote larger convective scales (Sakuraba & Roberts, 2009; Hori et al., 2012) and spatial variations along the boundary can influence the flow and efficiency of heat transfer, especially near the interface (e.g., Dietrich et al., 2016; Mound & Davies, 2017, for anomalies along the outer boundary). At extreme (i.e. realistic) parameters, however, the solutions for both thermal conditions appear to converge for rapidly rotating convection (Calkins et al., 2015) as well as Rayleigh-Bénard convection (Johnston & Doering, 2009). This convergence implies that convective-scale spatial variations in boundary heat flow have a secondary influence on the interior convection (Calkins et al., 2015). While significant effects may occur if the spatial scale of the thermal anomaly is comparable to the vertical scale of convection (e.g., Davies et al., 2009), it is unclear whether these effects will persist across the entire fluid depth (Davies & Mound, 2019).

Future numerical work should (1) strive for more realistic Ekman and Rayleigh numbers, (2) tackle the effect of boundary conditions, especially the Stephan-type condition at the top boundary due to melting/freezing of water along the interface and fixed heat flux along the bottom boundary, (3) consider both temperature and salinity buoyancy sources (e.g., Vance & Brown, 2005; Jansen, 2016), and (4) couple convectively and mechanically driven flows (e.g., Le Bars et al., 2015).

Future missions to the outer solar system may be able to better constrain the ocean flows and test the predictions of our calculations and convection models. Looking specifically to the Jovian system, the *Europa Clipper* and *JUICE* missions will determine the ocean thickness and salinity and may be able to place constraints on spatial variations of ice shell thickness (e.g., Phillips & Pappalardo, 2014; Grasset et al., 2013). Ice penetrating radar will provide information on ice shell thermophysical structure and constrain ice-ocean exchange processes (e.g., Kalousová et al., 2017), while magnetometer measurements may allow probing of ocean currents through their induction of magnetic fields (e.g., Tyler, 2011).

Acknowledgments
I thank Jonathan Aurnou, Baptiste Journaux, and Steve Vance for their helpful comments as well as Gabriel Tobie and Christophe Sotin for their constructive reviews. This work was supported by NASA Grant NNX14AR28G. Computational resources were provided by the NASA High-End Computing (HEC) Program through the NASA Advanced Supercomputing (NAS) Division at Ames Research Center. The MagIC code is publicly available at https://magic-sph.github.io/contents.html. All data is provided within the publication pages.

References

Abramson, E. H., Brown, J. M., & Slutsky, L. J. (2001). The thermal diffusivity of water at high pressures and temperatures. *J. Chem. Phys.*, *115*, 10461–10463.

Aubert, J., Brito, D., Nataf, H. C., Cardin, P., & Masson, J. P. (2001). A systematic experimental study of rapidly rotating spherical convection in water and liquid gallium. *Phys. Earth Planet. Int.*, *128*(1-4), 51–74.

Aurnou, J. M., Calkins, M. A., Cheng, J. S., Julien, K., King, E. M., Nieves, D., ... Stellmach, S. (2015). Rotating convective turbulence in earth and planetary cores. *Phys. Earth Planet. Int.*, *246*, 52–71.

Aurnou, J. M., & Heimpel, M. H. (2004). Zonal jets in rotating convection with mixed mechanical boundary conditions. *Icarus*, *169*, 492–498.

Aurnou, J. M., Heimpel, M. H., Allen, L., King, E. M., & Wicht, J. (2008). Convective heat transfer and the pattern of thermal emission on the gas giants. *Geophys. J. Int.*, *173*, 793–801.

Aurnou, J. M., Heimpel, M. H., & Wicht, J. (2007). The effects of vigorous mixing in a convective model of zonal flow on the Ice Giants. *Icarus*, *190*, 110–126.

Aurnou, J. M., & Olson, P. L. (2001). Strong zonal winds from thermal convection in a rotating spherical shell. *Geophys. Res. Lett.*, *28*(13), 2557–2559.

Baland, R.-M., Tobie, G., Lefevre, A., & Van Hoolst, T. (2014). Titan's internal structure inferred from its gravity field, shape, and rotation state. *Icarus*, *237*, 29–41.

Beuthe, M., Rivoldini, A., & Trinh, A. (2016). Enceladus's and Dione's floating ice shells supported by minimum stress isostasy. *Geophys. Res. Lett.*, *43*(19).

Bland, M. T., Showman, A. P., & Tobie, G. (2009). The orbital–thermal evolution and global expansion of Ganymede. *Icarus*, *200*(1), 207–221.

Brun, A. S., & Palacios, A. (2009). Numerical simulations of a rotating red giant star. I. Three-dimensional models of turbulent convection and associated mean flows. *Astrophys. J.*, *702*, 1078–1097.

Čadek, O., Souček, O., Běhounková, M., Choblet, G., Tobie, G., & Hron, J. (2019). Long-term stability of Enceladus' uneven ice shell. *Icarus*, *319*, 476–484.

Čadek, O., Tobie, G., Van Hoolst, T., Massé, M., Choblet, G., Lefèvre, A., ... others (2016). Enceladus's internal ocean and ice shell constrained from Cassini gravity, shape, and libration data. *Geophys. Res. Lett.*, *43*(11), 5653–5660.

Calkins, M. A., Hale, K., Julien, K., Nieves, D., Driggs, D., & Marti, P. (2015). The asymptotic equivalence of fixed heat flux and fixed temperature thermal boundary conditions for rapidly rotating convection. *J. Fluid Mech.*, *784*, R2.

Chandrasekhar, S. (1961). *Hydrodynamic and hydromagnetic stability.* Oxford: Clarendon.

Cheng, J. S., Aurnou, J. M., Julien, K., & Kunnen, R. P. J. (2018). A heuristic framework for next-generation models of geostrophic convective turbulence. *Geophys. Astrophys. Fluid Dyn.*, *112*(4), 277–300.

Choblet, G., Tobie, G., Sotin, C., Běhounková, M., Čadek, O., Postberg, F., & Souček, O. (2017). Powering prolonged hydrothermal activity inside Enceladus. *Nature Astron.*, *1*(12), 841.

Choukroun, M., & Sotin, C. (2012). Is Titan's shape caused by its meteorology and carbon cycle? *Geophys. Res. Lett.*, *39*(4).

Christensen, U. R. (2001). Zonal flow driven by deep convection on the major planets. *Geophys. Res. Lett.*, *28*, 2553–2556.

Collins, G., & Nimmo, F. (2009). Chaotic terrain on Europa. In R. T. Pappalardo, W. B. McKinnon, & K. K. Khurana (Eds.), *Europa* (p. 259-281). Tucson: University of Arizona Press.

Daly, M., Rack, F., & Zook, R. (2013). Edwardsiella andrillae, a new species of sea anemone from Antarctic Ice. *PloS one*, *8*(12), e83476.

Davies, C. J., Gubbins, D., & Jimack, P. K. (2009). Convection in a rapidly rotating spherical shell with an imposed laterally varying thermal boundary condition. *J. Fluid Mech.*, *641*, 335–358.

Davies, C. J., & Mound, J. E. (2019). Mantle-induced temperature anomalies do not reach the inner core boundary. *Geophys. J. Int.*, *218*, 2054–065.

DeRosa, M. L., Gilman, P. A., & Toomre, J. (2002). Solar multiscale convection and rotation gradients studied in shallow spherical shells. *Astrophys. J.*, *581*(2), 1356.

Dietrich, W., Hori, K., & Wicht, J. (2016). Core flows and heat transfer induced by inhomogeneous cooling with sub-and supercritical convection. *Phys. Earth Planet. Int.*, *251*, 36–51.

Dombard, A. J., & McKinnon, W. B. (2001). Formation of grooved terrain on Ganymede: Extensional instability mediated by cold, superplastic creep. *Icarus*, *154*(2), 321–336.

Dormy, E., Soward, A. M., Jones, C. A., Jault, D., & Cardin, P. (2004). The onset of thermal convection in rotating spherical shells. *J. Fluid Mech.*, *501*, 43–70.

Durante, D., Hemingway, D. J., Racioppa, P., Iess, L., & Stevenson, D. J. (2019). Titan's gravity field and interior structure after Cassini. *Icarus*, *326*, 123–132.

Ecke, R. E., & Niemela, J. J. (2014). Heat transport in the geostrophic regime of rotating Rayleigh-Bénard convection. *Phys. Rev. Lett.*, *113*, 114301.

Eicken, H., Oerter, H., Miller, H., & Graf, W. (1984). Textural characteristics and impurity content of meteoric and marine ice in the Ronne Ice Shelf, Antarctica. *J. Glaciol.*, *40*(135), 386–398.

Feistel, R. (2010). Extended equation of state for seawater at elevated temperature and salinity. *Desalination*, *250*, 14–18.

Figueredo, P. H., & Greeley, R. (2003). The Emerging Resurfacing History of Europa from Pole-to-Pole Geologic Mapping. In Mackwell, S. and Stansbery, E. (Ed.), *Lunar and Planetary Institute Science Conference Abstracts* (Vol. 34, p. 1017).

Fischer, P. D., Brown, M. E., & Hand, K. P. (2015). Spatially resolved spectroscopy of Europa: The distinct spectrum of large-scale chaos. *Astron. J.*, *150*(5), 164.

Gastine, T., Heimpel, M. H., & Wicht, J. (2014). Zonal flow scaling in rapidly-rotating compressible convection. *Phys. Earth Planet. Int.*, *232*, 36–50.

Gastine, T., & Wicht, J. (2012). Effects of compressibility on driving zonal flow in gas giants. *Icarus*, *219*, 428–442.

Gastine, T., Wicht, J., & Aubert, J. (2016). Scaling regimes in spherical shell rotating convection. *J. Fluid Mech.*, *808*, 690–732.

Gastine, T., Wicht, J., & Aurnou, J. M. (2013). Zonal flow regimes in rotating anelastic spherical shells: An application to giant planets. *Icarus*, *225*, 156–172.

Gastine, T., Wicht, J., & Aurnou, J. M. (2015). Turbulent Rayleigh–Bénard convection in spherical shells. *J. Fluid Mech.*, *778*, 721–764.

Gilman, P. A. (1977). Nonlinear dynamics of Boussinesq convection in a deep rotating spherical shell – I. *Geophys. Astrophys. Fluid Dyn.*, *8*, 93–135.

Gilman, P. A. (1978). Nonlinear dynamics of Boussinesq convection in a deep rotating spherical shell – II. *Geophys. Astrophys. Fluid Dyn.*, *11*, 157–179.

Gissinger, C., & Petitdemange, L. (2019). A magnetically driven equatorial jet in Europa's ocean. *Nature Astron.*, *1*.

Goodman, J. C. (2014). Flow of an alien ocean. *Nature Geosci.*, *7*, 8–9.

Grasset, O., Dougherty, M. K., Coustenis, A., Bunce, E. J., Erd, C., Titov, D., ... others (2013). JUpiter ICy moons Explorer (JUICE): An ESA mission to orbit Ganymede and to characterise the Jupiter system. *Planet. Space Sci.*, *78*, 1–21.

Hartkorn, O., & Saur, J. (2017). Induction signals from Callisto's ionosphere and their implications on a possible subsurface ocean. *J. Geophys. Res.*, *122*(11).

Heimpel, M. H., Aurnou, J. M., & Wicht, J. (2005). Simulation of equatorial and high-latitude jets on Jupiter in a deep convection model. *Nature*, *483*, 193–196.

Heimpel, M. H., Gastine, T., & Wicht, J. (2015). Simulation of deep-seated zonal jets and shallow vortices in gas giant atmospheres. *Nature Geosci.*, *9*(1), 19.

Hemingway, D., Nimmo, F., Zebker, H., & Iess, L. (2013). A rigid and weathered ice shell on Titan. *Nature*, *500*, 550–552. doi: 10.1038/nature12400

Hori, K., Wicht, J., & Christensen, U. R. (2012). The influence of thermo-compositional boundary conditions on convection and dynamos in a rotating spherical shell. *Phys. Earth Planet. Int.*, *196–197*, 32–48.

Jansen, M. F. (2016). The turbulent circulation of a Snowball Earth ocean. *J. Phys. Oceanogr.*, *46*(6), 1917–1933.

Johnston, H., & Doering, C. R. (2009). Comparison of turbulent thermal convection between conditions of constant temperature and constant flux. *Phys. Rev. Lett.*, *102*(6), 064501.

Jones, C. A. (2015). Thermal and compositional convection in the outer core. In *Treatise on geophysics* (Vol. 8, pp. 115–159). Elsevier.

Julien, K., Knobloch, E., Rubio, A. M., & Vasil, G. M. (2012). Heat transport in low-Rossby-number Rayleigh-Bénard convection. *Phys. Rev. Lett.*, *109*, 254503.

Kalousová, K., Schroeder, D. M., & Soderlund, K. M. (2017). Radar attenuation in Europa's ice shell: Obstacles and opportunities for constraining the shell thickness and its thermal structure. *J. Geophys. Res. Planets*, *122*(3), 524–545.

Kuang, W., & Bloxham, J. (1997). An earth-like numerical dynamo model. *Nature*, *389*, 371–374.

Kvorka, J., Cadek, C., Tobie, G., & Choblet, G. (2018). Does Titan's long-wavelength topography contain information about subsurface ocean dynamics? *Icarus*, *310*, 149–164.

Le Bars, M., Cebron, D., & Le Gal, P. (2015). Flows driven by libration, precession, and tides. *Annu. Rev. Fluid Mech.*, *47*, 163–193.

Lefevre, A., Tobie, G., Choblet, G., & Čadek, O. (2014). Structure and dynamics of Titan's outer icy shell constrained from Cassini data. *Icarus*, *237*, 16 – 28. doi: 10 .1016/j.icarus.2014.04.006

Lemasquerier, D., Grannan, A. M., Vidal, J., Cébron, D., Favier, B., Le Bars, M., & Aurnou, J. M. (2017). Libration-driven flows in ellipsoidal shells. *J. Geophys. Res. Planets*, *122*(9), 1926–1950.

Leonard, E. J., Patthoff, D. A., Senske, D. A., & Collins, G. C. (2018). The Europa Global Geologic Map. *LPI Contributions*, *2066*.

Lewis, E. L., & Perkin, R. G. (1986). Ice pumps and their rates. *J. Geophys. Res.*, *91*, 11756–11762.

Lucchita, B. K. (1980). Grooved terrain on Ganymede. *Icarus*, *44*(2), 481–501.

Lunine, J. I. (2017). Ocean worlds exploration. *Acta Astronautica*, *131*, 123–130.

Manneville, J.-B., & Olson, P. L. (1996). Banded convection in rotating fluid spheres and the circulation of the Jovian atmosphere. *Icarus*, *122*(2), 242–250.

McCord, T. B., Hansen, G. B., & Hibbitts, C. A. (2001). Hydrated salt minerals on Ganymede's surface: evidence of an ocean below. *Science*, *292*(5521), 1523–1525.

Melosh, H. J., Ekholm, A. G., Showman, A. P., & Lorenz, R. D. (2004). The tem-

perature of Europa's subsurface water ocean. *Icarus*, *168*, 498–502.

Miquel, B., Xie, J.-H., Featherstone, N., Julien, K., & Knobloch, E. (2018). Equatorially trapped convection in a rapidly rotating shallow shell. *Phys. Rev. Fluids*, *3*(5), 053801.

Mitri, G., Meriggiola, R., Hayes, A., Lefevre, A., Tobie, G., Genova, A., ... Zebker, H. (2014). Shape, topography, gravity anomalies and tidal deformation of Titan. *Icarus*, *236*, 169–177.

Moore, J. C., Reid, A. P., & Kipfstuhl, J. (1994). Microphysical and electrical properties of marine ice and its relationship to meteoric and sea ice. *J. Geophys. Res.*, *99*, 5171–5180.

Mound, J. E., & Davies, C. J. (2017). Heat transfer in rapidly rotating convection with heterogeneous thermal boundary conditions. *J. Fluid Mech.*, *828*, 601–629.

Nayar, K. G., Sharqawy, M. H., & Banchik, L. D. (2016). Thermophysical properties of seawater: a review and new correlations that include pressure dependence. *Desalination*, *390*, 1–24.

Nimmo, F. (2004). Non-newtonian topographic relaxation on Europa. *Icarus*, *168*, 205–208.

Nimmo, F., & Bills, B. G. (2010). Shell thickness variations and the long-wavelength topography of Titan. *Icarus*, *208*(2), 896–904.

Nimmo, F., & Pappalardo, R. T. (2016). Ocean worlds in the outer solar system. *J. Geophys. Res. Planets*, *121*(8), 1378–1399.

Nimmo, F., Thomas, P. C., Pappalardo, R. T., & Moore, W. B. (2007). The global shape of Europa: Constraints on lateral shell thickness variations. *Icarus*, *191*, 183–192.

Palguta, J., Anderson, J. D., Schubert, G., & Moore, W. B. (2006). Mass anomalies on Ganymede. *Icarus*, *180*, 428–441.

Pappalardo, R. T., & Barr, A. C. (2004). The origin of domes on Europa: The role of thermally induced compositional diapirism. *Geophys. Res. Lett.*, *31*, L01701.

Phillips, C. B., & Pappalardo, R. T. (2014). Europa Clipper mission concept: Exploring Jupiter's ocean moon. *Eos, Transactions American Geophysical Union*, *95*(20), 165–167.

Rovira-Navarro, M., Rieutord, M., Gerkema, T., Maas, L. R., van der Wal, W., & Vermeersen, B. (2019). Do tidally-generated inertial waves heat the subsurface oceans of Europa and Enceladus? *Icarus*, *321*, 126–140.

Sakuraba, M., & Roberts, P. H. (2009). Generation of a strong magnetic field using uniform heat flux at the surface of the core. *Nature Geosci.*, *2*, 802–805.

Schmidt, B. E., Blankenship, D. D., Patterson, G. W., & Schenk, P. M. (2011). Active formation of chaos terrain over shallow subsurface water on Europa. *Nature*, *479*, 502–505.

Soderlund, K. M., Heimpel, M. H., King, E. M., & Aurnou, J. M. (2013). Turbulent models of ice giant internal dynamics: Dynamos, heat transfer, and zonal flows. *Icarus*, *224*, 97–113.

Soderlund, K. M., Schmidt, B. E., Wicht, J., & Blankenship, D. D. (2014). Ocean-driven heating of Europa's icy shell at low latitudes. *Nature Geosci.*, *7*, 16-19.

Sotin, C., Head, J. W., & Tobie, G. (2002). Tidal heating of upwelling thermal plumes and the origin of lenticulae and chaos melting. *Geophys. Res. Lett.*, *29*(8), 1233, doi:10.1029/2001GL013884.

Travis, B. J., Palguta, J., & Schubert, G. (2012). A whole-moon thermal history model of Europa: Impact of hydrothermal circulation and salt transport. *Icarus*, *218*, 1006–1019.

Tyler, R. H. (2008). Strong ocean tidal flow and heating on moons of the outer planets. *Nature*, *456*, 770–773.

Tyler, R. H. (2011). Magnetic remote sensing of Europa's ocean tides. *Icarus*, *211*, 906–908.

Vance, S. (2017). vancesteven/planetprofile: Release for use in reproducing results submitted to journal of geophysical research: Planets. *Zenodo*, *https://doi.org/10.5281/zenodo.844131*.

Vance, S., & Brown, J. M. (2005). Layering and double-diffusion style convection in Europa's ocean. *Icarus*, *177*, 506–514.

Vance, S., & Goodman, J. C. (2009). Oceanography of an ice-covered moon. In R. T. Pappalardo, W. B. McKinnon, & K. K. Khurana (Eds.), *Europa* (p. 459-482). Tucson: University of Arizona Press.

Vance, S., Panning, M. P., Stahler, S., Cammarano, F., Bills, B. G., Tobie, G., ... Banerdt, B. (2018). Geophysical investigations of habitability in ice-covered ocean worlds. *J. Geophys. Res.*, *123*, 180–205.

Wicht, J. (2002). Inner-core conductivity in numerical dynamo simulations. *Phys. Earth Planet. Int.*, *132*, 281–302.

Wilson, A., & Kerswell, R. R. (2018). Can libration maintain Enceladus's ocean? *Earth Planet. Sci. Lett.*, *500*, 41 – 46. doi: 10.1016/j.epsl.2018.08.012

Zhang, K., & Schubert, G. (2000). Magnetohydrodynamics in rapidly rotating spherical systems. *Annu. Rev. Fluid Mech.*, *32*, 409–443.

Table 1. Properties of icy satellite oceans in dimensional units and non-dimensional parameters. Kinematic viscosity from Nayar et al. (2016), thermal diffusivity from Abramson et al. (2001), interior model properties ($R_S, D_{Ih}, D_{ocean}, q$) from Vance et al. (2018), and thermodynamic properties (ρ, C_p, α) at the mean ocean temperatures and pressures of the respective interior models from Vance (2017) for $MgSO_4$ (0 and 10 wt %) and B. Journaux (personal communication) for seawater. Two outer ice shell thicknesses and three ocean compositions are considered for Enceladus and Europa, while three outer ice shell thicknesses and two ocean compositions are considered for Titan and Ganymede.

	Enceladus	Titan	Europa	Ganymede
Gravitational acceleration, g [m/s^2]	0.1	1.4	1.3	1.4
Rotation rate, Ω [s^{-1}]	5.3×10^{-5}	4.6×10^{-6}	2.1×10^{-5}	1.0×10^{-5}
Kinematic viscosity, ν [m^2/s]	1.8×10^{-6}	1.8×10^{-6}	1.8×10^{-6}	1.8×10^{-6}
Thermal diffusivity, κ [m^2/s]	1.4×10^{-7}	1.8×10^{-7}	1.6×10^{-7}	1.8×10^{-7}
Satellite radius, R_S [km]	252	2575	1561	2631
Ice Ih thickness, D_{Ih} [km]				
Water	51, 10	141, 74, 50	30, 5	134, 70, 5
$MgSO_4$ 10 wt%	50, 10	149, 86, 58	30, 5	157, 95, 26
Seawater	50, 10	–	30, 5	–
Ocean thickness, D_{ocean} [km]				
Water	11, 53	130, 369, 420	97, 124	119, 361, 518
$MgSO_4$ 10 wt%	13, 63	91, 333, 403	103, 131	24, 287, 493
Seawater	12, 55	–	99, 126	–
Heat flux, q [mW/m^2]				
Water	16, 81	14, 18, 20	24, 119	16, 20, 107
$MgSO_4$ 10 wt%	16, 83	14, 17, 19	24, 123	15, 18, 25
Seawater	16, 82	–	23, 121	–
Density, ρ [10^3 kg/m^3]				
Water	1.00, 1.00	1.11, 1.14, 1.14	1.04, 1.04	1.11, 1.14, 1.14
$MgSO_4$ 10 wt%	1.11, 1.11	1.20, 1.23, 1.24	1.15, 1.14	1.19, 1.23, 1.24
Seawater	1.02, 1.02	–	1.07, 1.07	–
Specific heat capacity, C_p [10^3 J/kg/K]				
Water	4.2, 4.2	3.0, 3.5, 3.6	3.9, 3.9	3.0, 3.5, 3.7
$MgSO_4$ 10 wt%	3.6, 3.7	2.1, 2.5, 2.8	3.3, 3.5	2.1, 2.4, 3.0
Seawater	4.0, 4.0	–	3.8, 3.8	–
Thermal expansivity, α [10^{-4} K^{-1}]				
Water	$-0.5, -0.5$	2.3, 4.0, 4.2	1.9, 1.9	2.2, 4.0, 4.4
$MgSO_4$ 10 wt%	1.2, 1.3	0.4, 2.1, 2.7	2.1, 2.3	-0.1, 1.9, 3.2
Seawater	0.1, 0.1	–	2.5, 2.5	–
Prandtl number, $Pr = \nu/\kappa$	13	10	11	10
Ekman number, $E = \nu/\Omega D^2$	$10^{-10} - 10^{-11}$	$10^{-11} - 10^{-12}$	10^{-12}	$10^{-10} - 10^{-13}$
Rayleigh number, $Ra = \alpha g \Delta T D^3/\nu\kappa$	$10^{16} - 10^{19}$	$10^{19} - 10^{23}$	$10^{20} - 10^{22}$	$10^{20} - 10^{24}$
Radius ratio, $\chi = \frac{(R_S - D_{Ih})}{(R_S - D_{Ih} - D_{ocean})}$	$0.74 - 0.95$	$0.83 - 0.96$	$0.92 - 0.94$	$0.80 - 0.99$

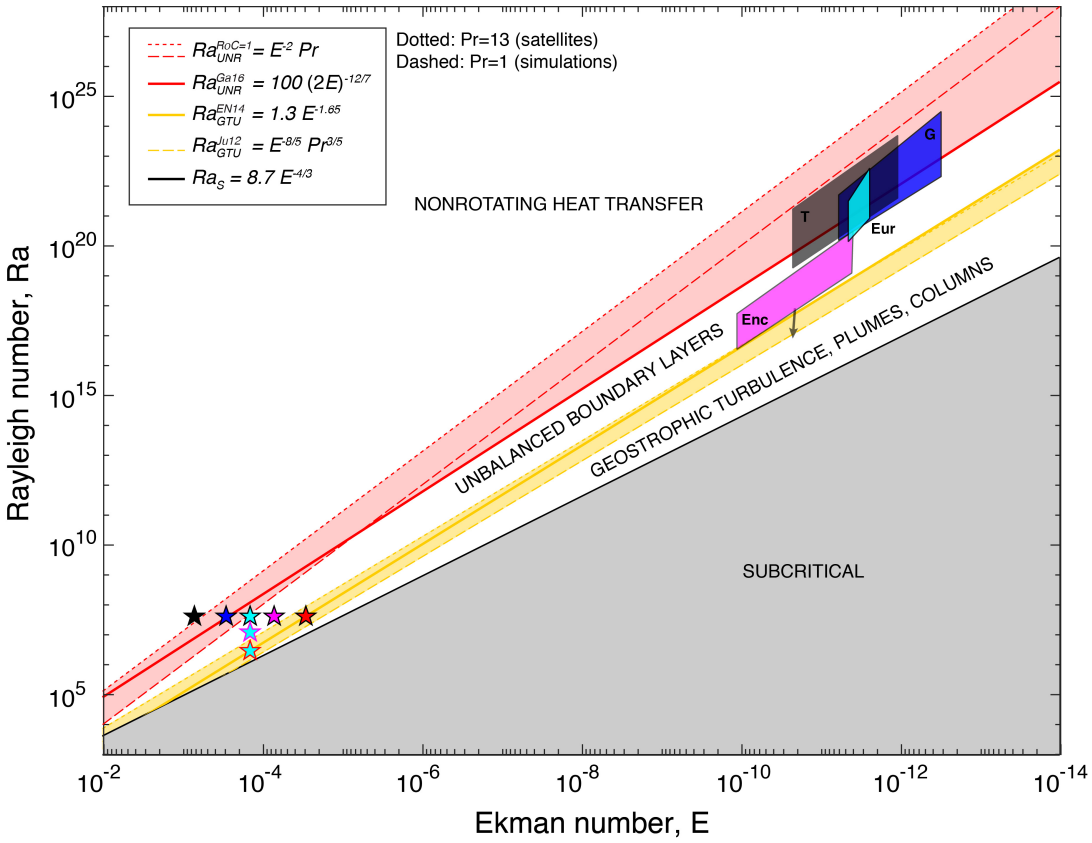

Figure 1. Convective regime diagram following Cheng et al. (2018) with superimposed parameter estimates for Enceladus (magenta), Titan (gray), Europa (cyan), and Ganymede (blue) superimposed (see Table 1). Our numerical simulations are denoted by stars, where interior color denotes Ekman number and exterior color denotes Rayleigh number. Interior: red ($E = 3.0 \times 10^{-5}$), magenta ($E = 7.5 \times 10^{-5}$), cyan ($E = 1.5 \times 10^{-4}$), blue ($E = 3.0 \times 10^{-4}$), and black ($E = 7.5 \times 10^{-4}$). Exterior: black ($Ra = 3.4 \times 10^{7}$), magenta ($Ra = 1.0 \times 10^{7}$), and red ($Ra = 2.4 \times 10^{6}$). The black line denotes the scaling for the onset of convection at Rayleigh number Ra_S (Chandrasekhar, 1961), the yellow lines bound the range of predicted transitions from the GT regime to the UBL regime that occurs at a Rayleigh number Ra_{GTU} (Ecke & Niemela, 2014; Julien et al., 2012), and the red lines bound the range of predicted transitions from the UBL regime to the NR regime that occurs at a Rayleigh number Ra_{UNR} (Gastine et al., 2016; Gilman, 1977). The $Ra_{UNR}^{RoC=1}$ and Ra_{GTU}^{EN14} scalings depend on the Prandtl number; dotted lines assume $Pr = 13$ following the upper estimate for icy satellite oceans while dashed lines assume $Pr = 1$ as used in the simulations.

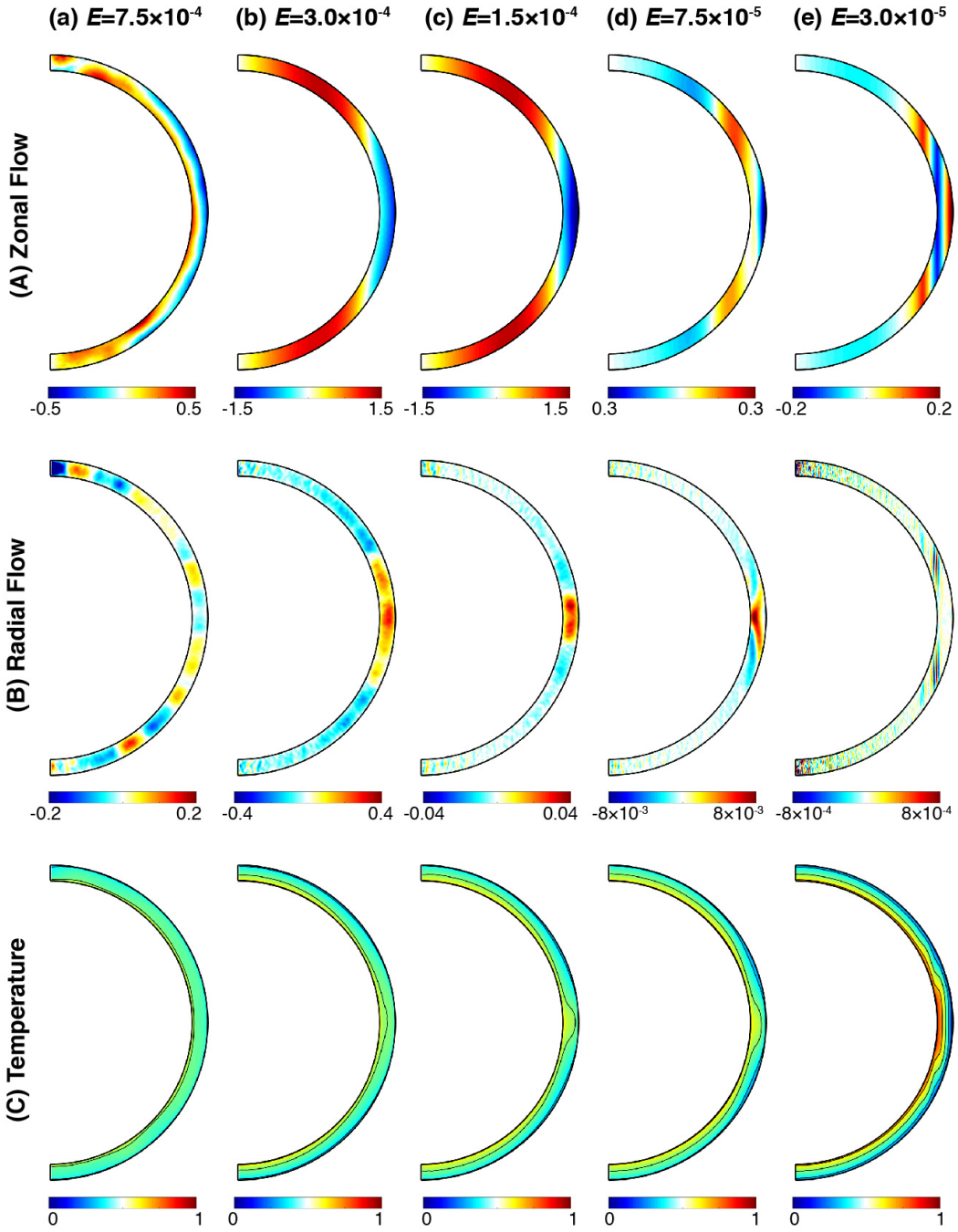

Figure 2. Mean velocity and temperature fields averaged over all longitudes and at least 0.02 viscous diffusion times for each model in the Ekman number suite. (A) Zonal flows given in dimensionless Rossby number units, $Ro = U/\Omega D$, which characterizes the ratio of rotational to inertial timescales. Red (blue) denotes prograde (retrograde) currents. (B) Radial flows given in Ro units. Red (blue) denotes upwelling (downwelling) currents. (C) Superadiabatic temperature in dimensionless units with isotherm contours superimposed (interval of 0.2). Red (blue) denotes warm (cool) fluid.

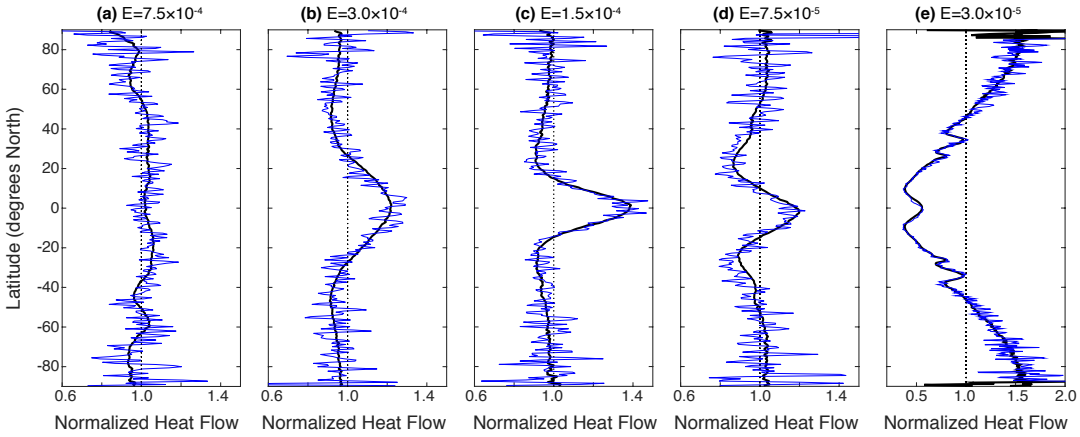

Figure 3. Heat flux along the outer boundary normalized by the mean value for each model in the Ekman number suite. Black lines denote the average over all longitudes and at least 0.02 viscous diffusion times; blue lines show azimuthal averages at snapshots in time.

Geophysical Research Letters

Supporting Information for

Ocean dynamics of outer solar system satellites

K. M. Soderlund

Institute for Geophysics, Jackson School of Geosciences, The University of Texas at Austin, Austin, Texas, USA

Contents of this file

Figures S1 to S3

Introduction

Below are three figures showing (1) the convective regime diagram from Figure 1 zoomed in on each satellite and the numerical models and (2) modeling results from the suite of numerical models that vary the Rayleigh number for fixed Ekman and Prandtl numbers.

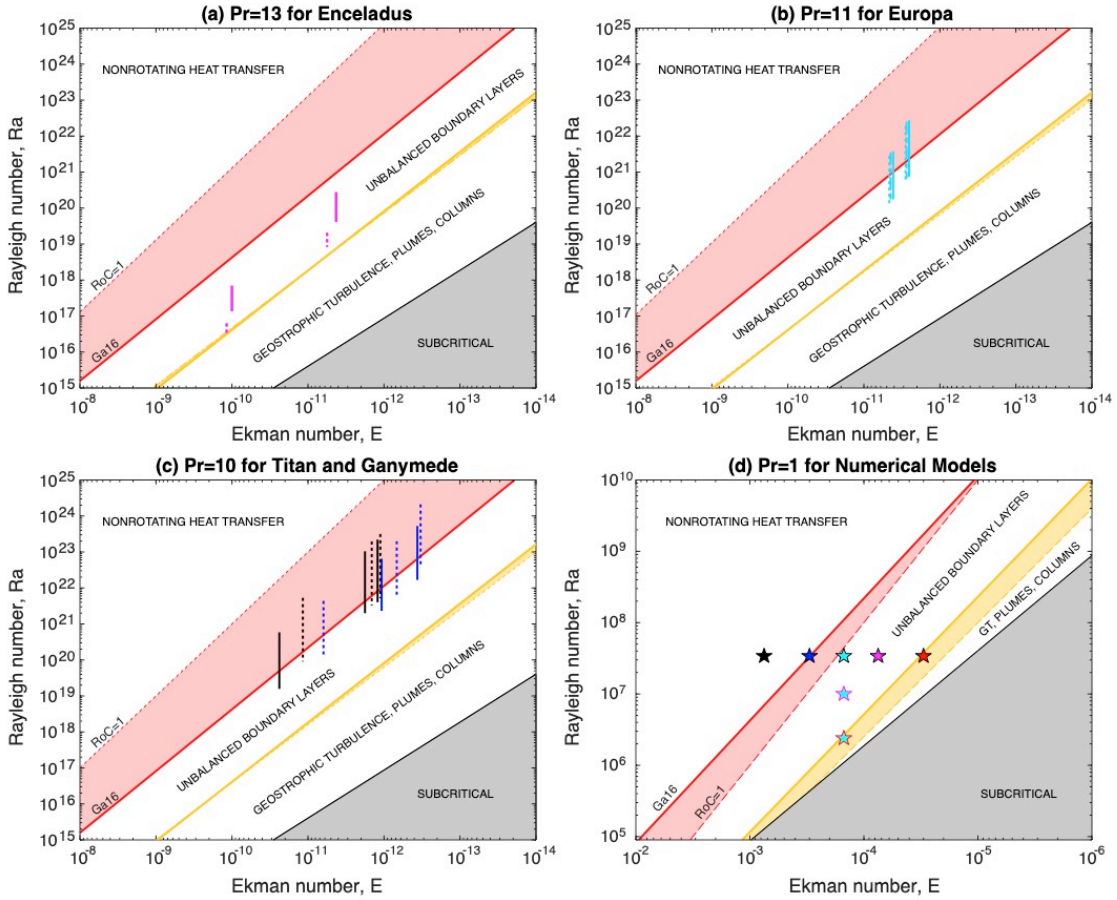

Figure S1. Convective regime diagram following Cheng et al. (2018) zoomed in on (a) Enceladus, (b) Europa, (c) Titan and Ganymede, and (d) the numerical models. In (a), magenta vertical lines denote the *Ra*-*E* estimates for Enceladus assuming thick and thin outer ice shells; solid lines denote an $MgSO_4$ (10 wt %) composition and dashed lines denote seawater. Pure water was also considered but has $\alpha<0$ and is therefore stable to convection. In (b), cyan vertical lines denote the *Ra*-*E* estimates for Europa assuming thick and thin outer ice shells; solid lines denote an $MgSO_4$ (10 wt %) composition, dashed lines denote seawater, and dotted lines denote pure water. In (c), black (blue) vertical lines denote the *Ra*-*E* estimates for Titan (Ganymede) assuming thick, intermediate, and thin outer ice shells; solid lines denote an $MgSO_4$ (10 wt %) composition and dotted lines denote pure water. In (d), numerical simulations are denoted by stars, where interior color denotes Ekman number and exterior color denotes Rayleigh number. Interior: red (E=3.0×10^{-5}), magenta (E=7.5×10^{-5}), cyan (E=1.5×10^{-4}), blue (E=3.0×10^{-4}), and black (E=7.5×10^{-4}). Exterior: black (Ra=3.4×10^{7}), magenta (Ra=1.0×10^{7}), and red (Ra=2.4×10^{6}). In all panels, the black diagonal line denotes the scaling for the onset of convection (Chandrasekhar, 1961), the yellow lines bound the range of predicted transitions from the GT regime to the UBL regime (Ecke & Niemela, 2014; Julien et al., 2012), and the red lines bound the range of predicted transitions from the UBL regime to the NR regime (Gastine et al., 2016; Gilman ,1977) using the same line conventions as Figure 1.

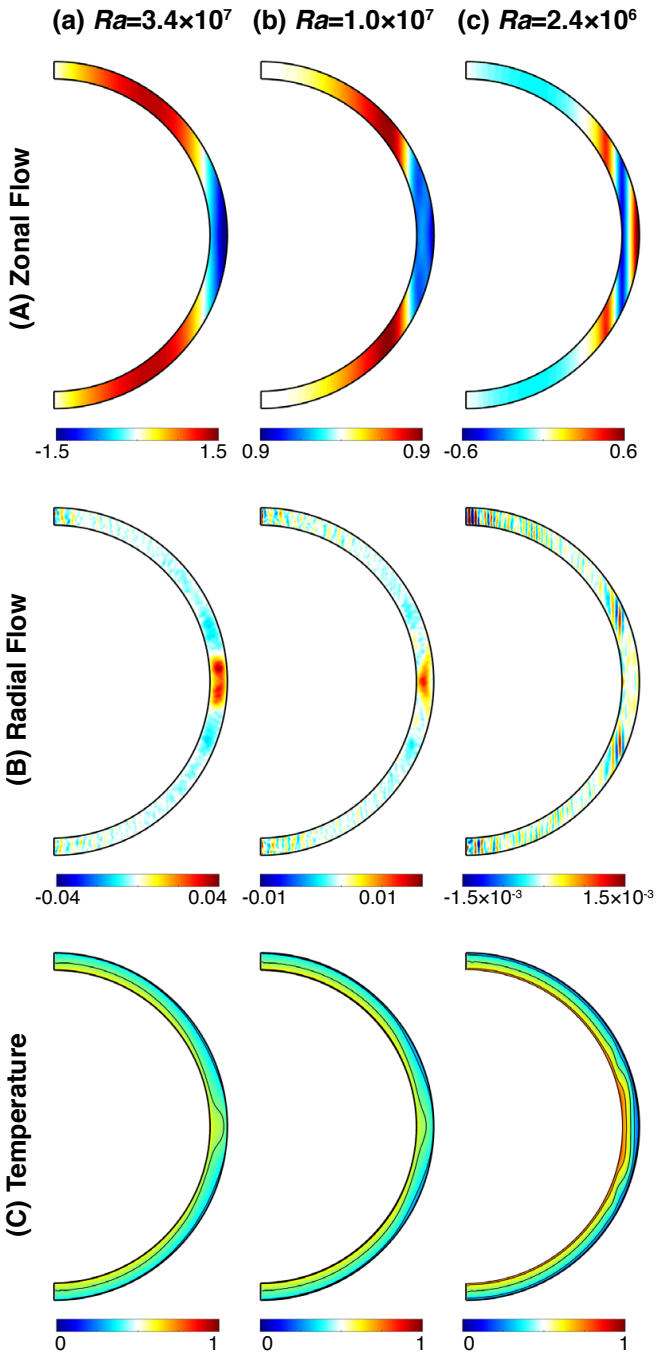

Figure S2. Mean velocity and temperature fields averaged over all longitudes and at least 0.02 viscous diffusion times for each model in the Rayleigh number suite. (A) Zonal flows given in dimensionless Rossby number units, $Ro=U/\Omega D$, which characterizes the ratio of rotational to inertial timescales. Red (blue) denotes prograde (retrograde) currents. (B) Radial flows given in *Ro* units. Red (blue) denotes upwelling (downwelling) currents. (C) Superadiabatic temperature in dimensionless units with isotherm contours superimposed (interval of 0.2). Red (blue) denotes warm (cool) fluid.

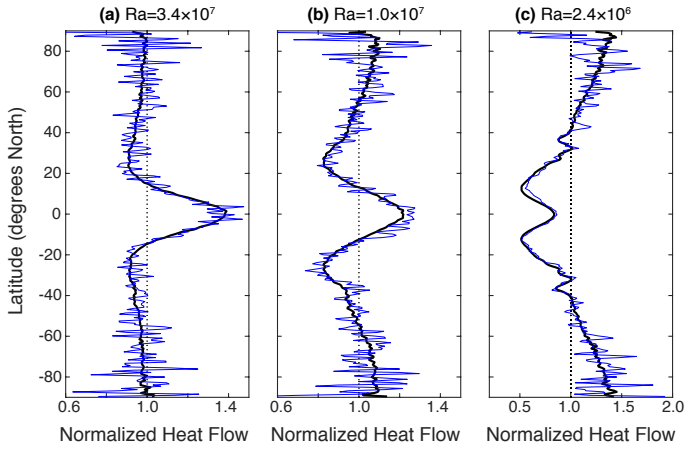

Figure S3. Heat flux along the outer boundary normalized by the mean value for each model in the Rayleigh number suite. Black lines denote the average over all longitudes and at least 0.02 viscous diffusion times; blue lines show azimuthal averages at snapshots in time.